

Unsteady onflow effects on model train drag

K. A. Weinman*¹ and K. Ehrenfried¹

[1] DLR Göttingen, Institute of Aerodynamics and Flow Technology,
Bunsenstr. 10, Göttingen 37073, Germany
keith.weinman@dlr.de

Abstract. The DLR NGT-Cargo concept aims to increase the rail share of the European freight traffic market. Computational Fluid Dynamics (CFD) is a useful tool in analysing high-speed operations which are an important part of this concept. Standards provide guidelines for CFD assessments at cross-wind conditions using the RANS (Reynolds-averaged Navier-Stokes) equations. The development of aerodynamic forces under unsteady on-flows should be analysed within the context of these standards. A major challenge in satisfying these guidelines arises because of the multi-scale nature of these flows which are characterized by a large range of energetically significant flow scales. Wind-tunnel measurements, focussed on the development of the aerodynamic forces acting on a train, are being currently performed on a 1:25 scaled NGT model in the cross-wind facility *Seitenwindversuchsanlage* Göttingen (SWG) located at the DLR Göttingen. A CFD study is running concurrently. The aim of this study is to assess the ability of CFD approaches to reproduce both the observed on-flow conditions as well as the aerodynamic drag of the vehicle.

1 Introduction

Stringent safety requirements over a wide range of operational conditions are applied to modern high-speed trains. Achieving this requires an understanding of the aerodynamic forces under cross-wind conditions. Measurement of force coefficients for full-scale vehicles is optimal but it is expensive. Normal practice is geared towards the use of small-scale models that can be tested inexpensively in wind-tunnel experiments or by using full-scale in-service vehicles [1]. Up till the present vehicle stability has been of paramount importance, but accurate assessments of vehicle aerodynamic forces under realistic conditions have become more relevant. The use of computational methods to assess the aerodynamic loading on trains has been recognized by the transport industry. The German standard EN 14067-6 [3] permits evaluation of aerodynamic forces for cross-wind conditions using CFD simulations for full-scale or reduced model geometries. Guidelines in EN 14067-6 for RANS methods are stringent. In particular the standard requires that computed integral forces cannot be accepted for certification work if variations against accepted reference values (i.e. experiment) differ by more than three percent. A major challenge in satisfying EN 14067-6 requirements is due to the multi-scale nature of the flow which is characterized by a large range of energetically significant flow scales. Geometrical features of a train, such as the underflow region, the train base [4, 5], the inter-car gaps (ICG's) and boogie cavities, generate small-scale

unsteady flow structures which interact with larger flow scales and can thereby influence the development of the aerodynamic forces. Figure 1 illustrates the contributions which comprise the total drag force. The skin friction and the pressure drag of the train head/tail dominate. Other contributions are smaller but no less important. The under-flow region contains numerous complex flow phenomena and is characterized typically by regions of flow separation driven by both geometry and incipient pressure gradient effects, together with cross-sectional area changes due to the underside geometry (e.g. inter-car gaps). In addition, the wake region [6] is dominated by vortex shedding events which contribute to the complexity of the modeling problem. Another contribution to the train aerodynamic force balance is provided by a steady vortex system originating from the front nose of the train [1, 7, 8] which contributes significantly to the form drag penalty [4].

Computational assessments of the flow about a train, traditionally undertaken on the basis of RANS methods, have not been totally satisfactory, for example [10] and [11] compared computational estimates of integral forces and moments using well-resolved meshes against the NGT2 experiment of [12]. Computations were performed for Reynolds numbers over the range R in $[250000, 750000]$ with cross-wind conditions of up to 30 degrees. The computed integral force and moment coefficients, particularly drag, demonstrated differences against experimental measurements of up to 15 percent. Large Eddy Simulation (LES), for example [8], has demonstrated improvements in comparison to RANS methods. [11] and [13] validated highly resolved RANS, URANS, LES, Delayed Detached Eddy Simulation (DDES), and Lattice Boltzmann (LBM) methods against [12]. This work demonstrated improvement for DDES, LES and the LBM methods against conventional RANS in the prediction of the aerodynamic pitching moment, however differences against the measured drag were unsatisfactory. As noted by [4] traditional RANS methods will retain their importance for the foreseeable future. These observations provided the motivation for a study on the mesh characteristics required for Reynolds Averaged Navier-Stokes methods under steady on-flow conditions [9] which identified the critical refinement area as the front nose of the vehicle. Vehicle aerodynamic loading under unsteady conditions were studied experimentally in [14] and [15]. Measurements were collected in-field under real conditions. These measurements were then replicated in wind-tunnel experiments whereby on-flow length and time scales were controlled using a set of oscillating flaps in front of the model. Two CFD methods were developed and validated against both of these experimental approaches [16]. The first method uses field reconstruction methods to construct on-flow boundary conditions that are representative of measured flow length and time scales. A second method uses sliding mesh techniques to model a set of oscillating flaps. The work presented in this paper follows the second method.

The paper is organized as follows. A brief overview of the train model is presented in section 2. The numerical method is discussed in section 3. A short overview of mesh properties is then introduced in section 4 following by an assessment of the current CFD calculations in section 5. Computational resources and conclusions are discussed in sections 6 and 7 respectively.

2 Train model and experiment setup

For this paper a model consisting only of the main train aerodynamic surfaces and the wind tunnel is considered. Additional features, such as inter-car gaps and bogey cavities, are included. Figure 2 shows the wind-tunnel model used in the experiment. The model is an 1:25 scale NGT-Cargo with a center wagon and two end wagons. The length of the model is 2.58 m. The reference co-ordinate system is stationary and coincides with the inertial reference frame of the wind tunnel. The model train height (L_h) is 200 mm with the train base having a width (L_b) of 125 mm. Passive/active suction is applied to control the on-flow boundary layer thickness in the experiment. To the left of the model the lower Prandtl probe can be seen. Its holder projects obliquely over the moving belt whose function is to simulate moving ground effects. The head of the probe is exactly 400 mm above the channel floor or the belt. The definition of the characteristic length for the Reynolds number within the industrial train research community is motivated by difficulties in comparing different vehicle configurations. For example, the height of single and double deck vehicles can vary significantly but the widths are approximately constant due to the standard rail gauge the vehicles must operate on. A reference width of 3 m at full scale is commonly used in Europe. The scaled reference width provides the reference length used to compute the Reynolds number for the wind-tunnel experiment. The Reynolds number is defined as Eq. (1),

$$R = \rho LU / \mu, \quad (1)$$

where U , ρ , μ , and L are the freestream velocity, fluid density, fluid dynamic viscosity and Reynolds length scale respectively. For this work the Reynolds number, based on L_b , is 200,000 for the selected wind-tunnel section velocity of 30 m/s. At present CFD simulations with and without flaps have been made. However passive and active suction have not yet been implemented into the computational model. Table 1 shows the measurement points chosen from the experimental program against which CFD comparisons are provided.

Experiment	Passive Suction	Active Suction	Flaps	Tunnel Bulk Velocity (m/s)
0020	Off	No	No	30
0023	On	No	0 Hz, 0 deg	30
0047	On	Yes	30 Hz, 3 deg	30

Table 1: Test conditions against which CFD results are compared.

3 The numerical method

The current work uses the Engys OpenFOAM releases 3.5.0/3.5.1. The baseline turbulence models used are the Menter $k-\omega$ SST [19], Spalart-Allmaras [21] and the $k-\epsilon$ [22] turbulence models. The DDES version of the Menter-SST turbulence model [20] is

used for hybrid RANS-LES calculations with the DDES filter width chosen as 2Δ [24], where Δ is the cube root of the cell volume. It must be noted that the DDES method implemented here is not intended to fully resolve the full range of turbulent structures and resolving about 50-60% of the turbulent kinetic energy (NRDDES), rather the intention is to reduce dissipation effects inside vortex cores and free-shear layers. The incompressible form of the momentum and continuity equations are written below:

$$\partial_t u + u \cdot \nabla u = -\frac{1}{\rho} \nabla p + \nu \nabla^2 u, \quad (2)$$

$$\nabla \cdot u = 0. \quad (3)$$

Justification for the choice of the incompressible form of the Navier-Stokes equations is given by the Mach number of the wind-tunnel flow ($M=0.0867$). Note that there are some flow regions about the model where the CFD shows that $M > 0.2$. However, these regions are considered to be at the upper range of the incompressible limit. Turbulence effects are conventionally modeled using an effective viscosity [18]. For RANS solutions the SIMPLE [17] algorithm is used to solve the discrete forms of Eqs. (2) and (3). Gradient, divergence, and Laplacian operators are second-order in space. Three non-orthogonal correction steps are performed per iteration and the solution is terminated when the residuals of the pressure correction equation, momentum equations, and turbulent viscosity equations are of $O(1e-10, 1e-8, 1e-7)$ respectively. If the averaged drag vector variations lie within a 99% confidence interval (CI) of $1.0e-6$ stochastic convergence is assumed. For unsteady calculations the PISO [23] method is used with second-order discrete spatial and temporal operators. A blended form of the inviscid flux operator is used to assist in reducing numerical dissipation effects for hybrid RANS-LES (DDES[20]). Boundary conditions used are specified in [9].

4 Mesh properties

Recommendations of [9] are closely followed. Surface length scales are of $O(2)$ mm, while control volume length scales vary from 2 mm near the vehicle to 15 mm inside the wind tunnel space. Wake regions for the flaps are resolved to a length scale of 3 mm up and including the train model. Native OpenFOAM mesh generation software is used. The Courant-Friedrichs-Lewy (CFL) number is limited to $O(1)$, leading to time steps of the order 10^{-6} seconds for unsteady calculations.

5 Assessment of the computed flow fields

For the work presented in this paper the flap motion is parameterized by frequency and amplitude respectively. Figure 3 illustrates the development of the flow field at three different values of height above the wind-tunnel floor using the Menter-SST turbulence model with stationary flaps. At one fifth of the model height the wakes to the left and right of the symmetry axis merge together (possibly due to Coanda and wake entrainment effects). As height above the tunnel floor is increased, four wakes can be seen

to convect downstream. Figure 4 shows the computed power spectral densities. Spectra have been averaged over 30 convective time units and a low pass Hanning filter is applied. The amount of noise in the experiment is significant and a known signal is required to properly filter the data. The signal chosen is that of the flap oscillation so that flow spectra for the case where the flaps are stationary cannot yet be provided. Force components exhibit a peak near 3 Hz with indications of a higher mode at 6 Hz. F_z shows a peak at about 25 Hz while F_y contains two modes at about 12 and 45 Hz. The 25 Hz peak is related to the moving belt and matches experimental observation. A timescale derived from the model length and the test section velocity matches the 12 Hz mode so that this mode is flow related. However this mode matches a rotational eigenfrequency of the model/spear suggesting possible coupled flow-structure interaction. The 45 Hz signal corresponds to the Strouhal number observed for vortex shedding for bodies of aspect ratio greater than 2. The CFD overestimates this mode by about 14% - this is characteristic for non-resolving methods. In Figure 5 (left) the flow is shown at one instant and the flap motion is parameterized by 30 Hz/3 degrees. Merging of the inboard and outboard wakes is seen again and disappears as height above the floor is increased. Figure 6 (right) illustrates the development of the fluctuating aerodynamic force coefficients over 25 convective time units. Since $L_b = 1/8$ m and both the forcing frequency and the bulk velocity share the same magnitude (30 Hz/30 m/s), a total angular rotation of 2π radians corresponds to eight convective time units and it is easy to see that F_y mirrors the flap oscillation. The aerodynamic forces appear to respond linearly to on-flow changes, supporting the observations of [14, 15] and [16]. Current CFD assessments of the integral forces are given in Table 2. Comparison is provided against preliminary experimental data. For this work a drag count (dct) is defined as $1000C_d$ where C_d is the drag force normalized by the product of the reference dynamic pressure and the projected area of the train head in the mean flow direction. All simulations include the moving belt which simulates relative ground motion. The table is divided into 5 groups, each representing the different assessments made. In group (a) RANS computations are performed in the wind tunnel without the flap geometry (experiment 0020). A variation of approximately O(58) dcts between the Menter-SST turbulence model result and the experiment (0020) is observed. For the Spalart-Allmaras and $k - \epsilon$ models the difference rises to O(100) dcts. The magnitudes of the computed yaw force (F_y) are in general agreement. However, there are differences in the magnitude of the lift force F_z . These are related to the turbulence models (since the mesh and numerical schemes are identical). The value of y^+ used in this study is optimized using a flat-plate boundary layers calculation with the Menter-SST model. It is considered that slight differences in the respective wall-function models within the y^+ range used can contribute to these differences. In order to demonstrate the importance of the near-wall resolution with regard to the computational force estimates, a series of calculations were carried out using meshes for which the near wall boundary layer is not well resolved. Results for these meshes are given in group (b) of the table. It can be seen that y^+ values are approximately four times larger and drag estimates are subsequently degraded. While uncertainty in experimental values plays a small role, variations between the CFD and experiment are most likely due to inadequate predictions of boundary layer separation and vortex breakdown [18].

Turbulence Model	Experiment	F_X	C_d	F_Y	F_Z	$F_{x,rms}$	$\langle y^+ \rangle$
Group (a): RANS without flaps and a resolved near-wall mesh.							
Menter-SST	0020	5.644	0.518	0.008	-0.515	-	16
$k - \epsilon$	0020	6.480	0.595	-0.048	-0.386	-	16
SA	0020	6.425	0.590	0.024	-0.100	-	16
Group (b): RANS without flaps with an unresolved near-wall mesh.							
Menter-SST	0020	6.150	0.564	-0.101	-0.290	-	63
$k - \epsilon$	0020	6.822	0.626	-0.098	-0.743	-	63
SA	0020	6.446	0.591	0.214	-0.070	-	64
Group (c): URANS with flaps (0 Hz, 0 deg) and a resolved near-wall mesh.							
Menter-SST	0023	6.267	0.575	-0.0788	-1.586	0.154	18
$k - \epsilon$	0023	7.000	0.642	-0.051	-0.951	0.029	16
SA	0023	6.545	0.601	0.0361	-1.9031	0.159	18
Group (d): DDES with flaps(0 Hz, 0 deg) and a resolved near-wall mesh.							
Menter-SST	0023	6.271	0.581	0.075	-1.591	0.506	18
Group (e): DDES with flaps (30 Hz, 3 deg) and a resolved near-wall mesh.							
Menter-SST	0047	7.127	0.654	0.024	-2.166	0.361	18
Experimental Points							
0020	-	5.0	0.46	-	-	-	-
0023	-	4.7	0.43	-	-	-	-
0047	-	5.3	0.49	-	-	0.35	-

Table 2: Comparison of force estimates (F) against selected experimental points. Force units are in Newtons. Note that the average dimensionless wall distance on the train model body is given by $\langle y^+ \rangle$.

Groups (c) and (d) include the effect of the stationary flap system (experiment 0023). In comparison to the system without flaps, the drag count increases by about 41 dcts on average for all models which corresponds to the experiment which shows a rise of 30 dcts. There is an increase of 74 drag counts when the flaps are activated (measurement 0047). This corresponds to the 60 dcts increase observed for the experiment (difference between measurements 0023 and 0047). However adding flaps to the system shows a measured drop of 30 dcts while the CFD shows an increase of all models. Additional analysis is required to clarify this discrepancy. The preliminary agreement between the experimental data set 0047 and the DDES methods is acceptable. URANS/RAN methods underestimate the measured root mean square (RMS) drag values and results shown here show that resolving flow methods are needed if second or higher statistical moment data are required. However, it is possible to determine cost-effective and useful flow information with the general approach presented in this paper.

6 Computational resources

Resources of the Cluster for Advanced Research in Aerospace (Dresden (CARA), Göttingen (CARO)) are used for the work presented in the paper. All work was performed on CARA until CARO became operational. Wall clock time scales at about 6.6×10^{-3} seconds per grid point per equation on CARA and about 5.0×10^{-4} seconds per grid point per iteration on the CARO cluster. This reflects hardware and other improvement that are present in the more recent CARO cluster.

7 Conclusions

Investigations are undertaken to validate CFD methods against experiments studying the influence of a time-dependent inflow on the aerodynamic drag of a 1:25 scaled model train. Both steady and unsteady on-flow conditions are considered. An oscillating flap system is used to control the amplitude and frequency of on-flow oscillations. This approach allows computationally efficient CFD modeling if the disturbances are constructed of only a few frequency modes. NRDES methods show superior performance to URANS for the cases studied at an equivalent computational cost. The NRDES based estimates of the aerodynamic force coefficients provide a better match against the measured drag but are unable to exactly capture the measured Strouhal number associated with vortex shedding about the model. It is felt that the differences seen in the Strouhal frequencies are due to modeling deficiencies (i.e flow is not fully resolved) and weaknesses in the numerical approach taken - for example symmetry preserving schemes have not yet been implemented into the modeling framework. The CFD identified flow modes at 12 Hz and at 25Hz which have the potential to excite flow-structure interaction: this work shows that there is some benefit in using an appropriate CFD method to identify potential problems and locations for experimental investigations. The CFD and experiment return qualitatively similar behavior in the drag response to on-flow conditions which suggest that these approaches can be complementary in achieving a deeper understanding of these flows.

8 Acknowledgement

The authors would also like to acknowledge Frau Annika Köhne for her assistance in the preparation of this paper.

References

1. Baker, C. (2010), The flow around high speed trains. *J. Wind Engineering and Industrial Aerodynamics*, 98(6), pp. 277-298
2. Orellano, A. (2010). *Aerodynamics of High Speed Trains*. Vehicle Aerodynamics lecture, Stockholm KTH.

3. DB Netz AG., Richtlinie 807.04 Bautechnik, Leit-, Signal- und Telekommunikationstechnik (2010). Ausgewählte Maßnahmen und Anforderungen and das Gesamtsystem Fahrweg/Fahrzeug Aerodynamik/Seitenwind, Frankfurt
4. Sima, M., Gurr, A., and Orellano, A. (2008), Validation of CFD for the flow under a train with 1:7 scale wind tunnel measurements, BBAA IV International Colloquium on Bluff Bodies Aerodynamics and Applications(9), pp. 1638-1649
5. Jönsson M., Wagner C. and Loose S. (2014), Particle image velocimetry of the underfloor flow for generic high-speed train models in a water towing tank, Proceedings of the Institution of Mechanical Engineers, Part F: Journal of Rail and Rapid Transit, 2014;228(2):194-209
6. Muld T.W. (2012), Slipstream and flow structures in the near wake of high-speed trains, Royal Institute of Technology, Department of Aeronautical and Vehicle Engineering, Stockholm, Sweden
7. Baker, C. (2014), A review of train aerodynamics: Part 1 - Fundamentals, The Aeronautical Journal, Volume 118, Issue 1201, pp. 201 - 228
8. Hemida, H. N (2006), Large-Eddy Simulation of the Flow around Simplified High-Speed Trains under Side Wind Conditions, Engng, Division of Fluid Dynamics, Dept. of Applied Mechanics, Chalmers University of Technology, Göteborg, Sweden
9. Weinman, K.A., Fragner, M.M., Deiterding, R., Heine, D., Fey, U., Braenstroem, F., Schultz, B. and Wagner, C. (2018), Assessment of the mesh refinement influence on the computed flow-fields about a model train in comparison with wind tunnel measurements Journal of Wind Engineering and Industrial Aerodynamics, 179, 102-117.
10. Weinman, K.A., Fey, U., Loose, S., Wagner, C., Deiterding, R. and Fragner, M. (2013), Comparison between CFD and Wind Tunnel experiment for slender bodies of aspect-ratio O1 in the presence of cross-wind, 10th World Conference on Railway Research
11. Fragner, M. M., Weinman, K.A., Deiterding, R., Fey, U. and Wagner, C., Comparison of industrial and scientific CFD approaches for predicting cross wind stability of the NGT2 model train geometry, Int. J. Railways Techn., 2015, 4(1), pp 1-18
12. Haff, J., Richard, U., Kowalski, T., Loose, S., and Wagner, C (2012), Wind Tunnel Experiments with a High-Speed Train model subject to Cross-Wind Conditions, Proceedings on the first international conference on Railway Technology: Research, Development and Maintenance (24), J.Pombo, Civil-Comp Press, Stirlingshire, Scotland
13. Fragner, M. M., and Deiterding, R. (2016), Investigating cross-wind stability of high speed trains with large-scale parallel CFD, Int. J. Comput. Fluid Dynamics, 30(6), pp 402-407
14. Wilhelmi, H. et al. (2020), Aerodynamic characterization of a compact car overtaking a heavy vehicle, New Results in Numerical and Experimental Fluid Mechanics XII. Notes on Numerical Fluid Mechanics and Multidisciplinary Design. Springer, Cham. ISBN 978-3-030-25252-6, no. 794804
15. Wilhelmi, H., et al. (2020), Simulation of transient on-road conditions in a closed test section wind tunnel using a wing system with active flaps. SAE Int. J. Passeng. Cars Mech. Syst. (0688), 1-13, ISSN 1946-3995
16. Weinman, K.A., Wilhelmi, H., Bell, J.R., Heine, D., Wagner, C. (2021). On the Simulation of a Heavy Vehicle Wake in OpenFOAM with Real-World Data. In: Dillmann, A., Heller, G., Krämer, E., Wagner, C. (eds) New Results in Numerical and Experimental Fluid Mechanics XIII. STAB/DGLR Symposium 2020. Notes on Numerical Fluid Mechanics and Multidisciplinary Cham.
17. Patankar, S.V. and Spalding, D.B. (1971), A Calculation Procedure for Heat, Mass and Momentum Transfer in Three-Dimensional Parabolic Flows. International Journal of Heat and Mass Transfer, 15(10), pp. 1787-1806
18. Wilcox, D.C. (2006), Turbulence Modeling for CFD, 3rd Edition, DCW Industries, Canada, CA, USA.

19. Menter, F.R., Kuntz, M. and Langtry, R. (2003), Ten Years of Industrial Experience with the SST Turbulence Model, Proceedings of the 4th International Symposium on Turbulence, Heat and Mass Transfer, Begell House Inc., West Redding, pp. 625-632.
20. Strelets, M. (2001), Detached Eddy Simulation of Massively Separated Flows, 39th AIAA Aerospace Sciences Meeting and Exhibit, Reno, NV
21. Spalart, P. R. and Allmaras, S. R. (1994), A One-Equation Turbulence Model for Aerodynamic Flows, Recherche Aérospatiale, No. 1, pp. 5-21.
22. Bardina, J.E., Huang, P.G., Coakley, T.J. (1997), Turbulence Modeling Validation, Testing, and Development, NASA Technical Memorandum 110446.
23. R. I. Issa (1985), Solution of the Implicitly Discretized Fluid Flow Equations by Operator-Splitting, Journal of Computational Physics, 62, pp 40-65
24. K. Weinman, H. van der Ven, C. Mockett, T. Knopp, J. Kok, R. Perrin, and F. Thiele. A study of grid convergence issues for the simulation of the massively separated flow around a stalled airfoil using DES and related methods. In P. Wesseling, E. Oñate, and J. Périaux, editors, Proceedings of the European Conference on Computational Fluid Dynamics ECCOMAS CFD 2006, Egmond aan Zee, The Netherlands, 2006.

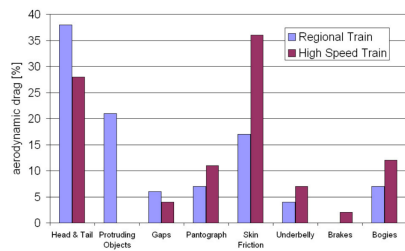


Fig. 1: Contributions to the aerodynamic drag of a train [2]



Fig. 2: The figure shows the NGT model inside the wind-tunnel.

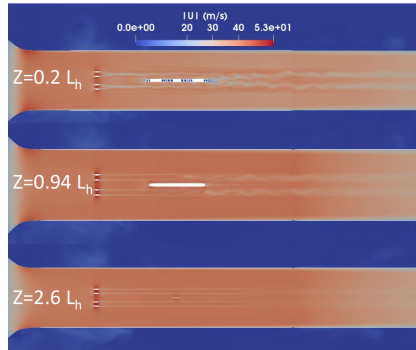


Fig. 3: Instantaneous snapshot of the velocity magnitude obtained for the CFD simulation of experiment 0023. The figure shows xy planes located at $z/L_h = [0.2, 0.94, 2.6]$ respectively.

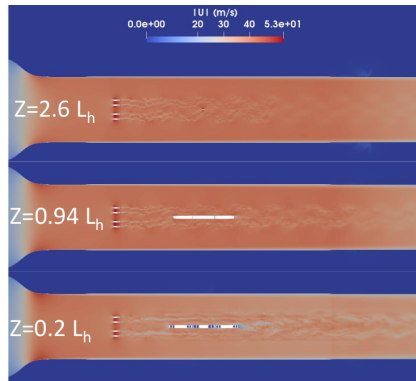


Fig. 5: Instantaneous snapshot of the velocity magnitude obtained for the CFD simulation of experiment 0047. The figure shows xy planes located at $z/L_h = [0.2, 0.94, 2.6]$ respectively.

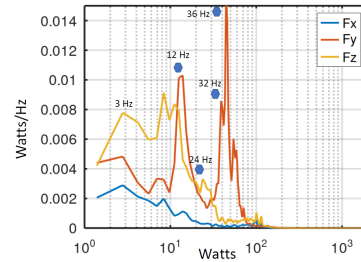


Fig. 4: The figure presents the averaged force coefficient spectra for the CFD simulation of experiment 0023. Blue symbols illustrate measured spectra for an experiment with a flap oscillation of 3 Hz. Labels indicating frequency are presented.

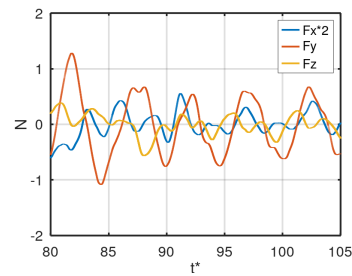


Fig. 6: The figure illustrates the development of the force coefficients obtained for the CFD simulation of experiment 0047.